RSC Advances

PAPER

View Article Online
View Journal | View Issue

Cite this: *RSC Adv.*, 2021, **11**, 12022

Hollow carbon-based nanosystem for photoacoustic imaging-guided hydrogenothermal therapy in the second near-infrared window†

Zhuo Jia,‡[a] Rong Dai,‡[abc] Ziliang Zheng,‡[bc] Yufei Qin,[bc] Ailin Duan,[bc] Xiaoyang Peng,[bc] Xianmei Xie *[a] and Ruiping Zhang *[c]

Compared with the near-infrared-I spectral window (NIR-I, 650–950 nm), a newly developed imaging and treatment window with a 1000–1700 nm range (defined as the NIR-II bio-window) has attracted much attention owing to its higher spatiotemporal resolution, increased tissue penetration depth and therapeutic efficacy. Herein, we designed a nanotheranostic platform (HC-AB NPs) *via* loading ammonia borane (AB) into hollow carbon nanoparticles (HCs) for NIR-II photoacoustic (PA) imaging-guided NIR-II hydrogenothermal therapy. Importantly, by exploiting the characteristics of beta zeolite as a hard template and a template-carbonization-corrosion process, the prepared HCs have excellent NIR-II absorption performance and AB loading capacity. With the high biocompatibility of HC-AB NPs, an efficient synergistic anti-tumor strategy has been achieved *via* high intratumoural accumulation and acid-stimulated H_2 release as well as PA-guided precise NIR-II photothermal therapy. The HC-AB NPs as a promising nanotheranostic platform opens a new avenue for high-efficacy NIR-II hydrogenothermal therapy.

Received 6th January 2021
Accepted 14th March 2021

DOI: 10.1039/d1ra00093d

rsc.li/rsc-advances

1. Introduction

Although traditional cancer therapies, including surgical therapy, chemotherapy and radiation therapy are clinically effective in fighting cancer, they can trigger numerous deleterious side effects.[1,2] Recently, as a promising alternative or supplementary method to traditional cancer therapies, photothermal therapy (PTT) with the characteristics of non-invasiveness, strong specificity, and high tumor eradication efficiency has attracted significant attention.[3,4] It is well known that PTT utilizes light energy to induce localized heat in tissue and destroy cancer cells.[5–8] Based on its deep tissue penetration capacity and negligible damage to normal tissues near-infrared (NIR) light stands out as one of the most commonly used light sources for high-efficiency PTT.[9,10] Compared with conventional NIR window I (NIR-I, 700–1000 nm), light in the second near-infrared optical window (NIR-II, 1000–1700 nm) has deeper light transmission inside tissue and higher maximum permissible exposure (MPE) to the laser.[11–13] Therefore, NIR-II-mediated PTT (NIR-II PTT) is a promising treatment strategy that utilizes the hyperthermia to ablate tumors. For this purpose, many nanomaterials with the favorable NIR-II light absorption ability, such as plasma metal clusters, semiconductor copper sulfide nanoparticles and carbon nanomaterials, have been exploited in NIR-II PTT.[14–17] Especially, carbon-based nanomaterials have received widespread attention due to their easy fabrication, long-term stability, strong NIR absorption and high photothermal conversion efficiency.[18,19] Nevertheless, the current NIR-II PTT has the disadvantage of uneven heat distribution, tumor recurrence and damage to normal tissues, or single therapy, which significantly hamper its clinical translation.[20–23]

Currently, synergistic therapy as a novel strategy has become a hotspot for enhancing anticancer efficacy, whether in clinical judgment and scientific research.[24–26] Studies have shown that the hyperthermia generated by PTT usually destroys the integrity of cell membranes to cause the release of intracellular reactive oxygen species (ROS) and trigger proinflammatory reactions *in vivo*, which consequently stimulates tumor regeneration and spread.[27,28] This clearly shows that inhibiting inflammation is very necessary for photothermal treatment of cancers. Therefore, an emerging gas therapy that uses gasotransmitters including H_2, NO, CO, H_2S and others to induce cancer cell apoptosis has attracted our attention.[29–31] Specifically, the H_2, an endogenous gasotransmitter, can destroy redox homeostasis of tumor cells *via* reacting with endogenous ROS

[a]*College of Chemistry and Chemical Engineering, Taiyuan University of Technology, Taiyuan 030024, China. E-mail: xxmsxty@sina.com*

[b]*Department of Biochemistry and Molecular Biology, Shanxi Medical University, Taiyuan 030001, China*

[c]*Department of Radiology, Third Hospital of Shanxi Medical University, Taiyuan 030032, China. E-mail: zrp_7142@sxmu.edu.cn*

† Electronic supplementary information (ESI) available. See DOI: 10.1039/d1ra00093d

‡ Z. Jia, R. Dai, and Z. Zheng contributed equally to this work.

Table 1 List of abbreviations

NIR-I	Near-Infrared-I
NIR-II	Near-infrared-II
PA	Photoacoustic
PTT	Photothermal therapy
GT	Gas therapy
ROS	Reactive oxygen species
EPR	Enhanced permeability and retention
HC	Hollow carbon
HC-AB NPs	Hollow carbon-ammonia borane nanoparticles

such as $^{\bullet}OH$ to form H_2O. In addition, H_2 can also inhibit inflammatory tissue damage caused by oxidative stress to down-regulating proinflammatory cytokines and other inflammatory mediators.[32,33] Therefore, synergetic hydrogenothermal therapy combining PTT with hydrogen therapy will be of great potential in overcoming cancer to achieve the therapeutic effect of "1 + 1 > 2". Recently, research on hydrogenothermal therapy has been carried out in an orderly manner. Zhang and co-workers developed a biomembrane-camouflaged nanomedicine (mPDAB) containing polydopamine and ammonia borane to enhance PTT efficacy and mitigate inflammation.[34] Zhao's group synthesized a cubic Pd nanocrystal for tumor-targeted and photoacoustic (PA) imaging-guided hydrogenothermal therapy of cancer.[35] However, the therapeutic applications of NIR-II for hydrogenothermal therapy has rarely been reported. Therefore, it is great of interest to explore an H_2 delivery nanocarrier with excellent properties in the NIR-II window.

Herein, we developed a novel hollow carbon-based nanoparticles (HC-AB NPs) modified by solid hydrogen storage material ammonia borane (AB) as a multifunctional hydrogenothermal agent for effectively tumor ablation, which has excellent PA imaging and anti-tumor effect in the NIR-II window (Scheme 1). The hollow carbon nanoparticles were firstly prepared on the basis of beta zeolite through template-carbonization-corrosion process,[36–38] and then the AB is loaded on the as-synthesized hollow carbon (HC) to obtain hollow carbon–ammonia borane nanoparticles (HC-AB NPs). Based on the enhanced permeability and retention (EPR) effect, the HC-AB NPs could provide more opportunities to passively accumulate into the tumor. Once internalized into cancer cells with the acidic tumor-microenvironment, the HC-AB NPs undergoes a stimulus-response process to produce H_2,[39] meanwhile the heat generated during NIR-II PTT can promote the release of H_2. Moreover, the obtained H_2 can not only be used for gas therapy (GT), but also reduce inflammatory damage caused by PTT. Therefore, the HC-AB NPs is expected to become a novel NIR-II hydrogenothermal therapy nanosystem guided by NIR-II PA imaging (Table 1).

2. Materials and methods

2.1 Materials

Tetraethylammonium hydroxide (TEAOH) and 1-butyl-3-methylimidazolium bromide (BMIMBr) were purchased from Shanghai Aladdin Biochemical Technology Co., Ltd. Sodium hydroxide (NaOH) and sodium aluminate ($NaAlO_2$) were bought from Sinopharm Chemical Reagent Beijing Co., Ltd. Ammonia borane (AB) were bought from Xiya Chemical Technology (Shandong) Co., Ltd. Fumed silica were purchased from Shanghai Macklin Biochemical Co., Ltd. All chemicals used here without further purification. DI water was acquired from a Milli-Q water purification system (Millipore, Bedford, MA) throughout the whole experiment.

2.2 Characterization

Transmission electron microscope images (TEM) were obtained on the Tecnai G2 F20 S-twin transmission electron microscopy, and morphology of the HC-AB NP were observed through the image. Dynamic light scattering (DLS) size distribution and zeta potential of samples were analyzed by a Nano Zetasizer (Malvern Instruments Ltd.). X-ray photoelectron spectroscopy (XPS) was obtained on a V. G. Scientific ESCALAB250 spectrometer with Al Kα radiation (1486.6 eV, 150 W). The UV-vis absorption spectra was obtained using a TU-1901 dual-beam UV-vis spectrophotometer (PerkinElmer), and NIR-II absorption spectrum was recorded by NIR2000 SPECTROMETER spectrum analyzer. Fourier-transform infrared (FT-IR) spectroscopy were obtained on a ALPHA II spectrophotometer (Bruker), using the KBr pellet technique. N_2 adsorption–desorption isotherms were tested on a Micromeritics ASAP 2020 system, the BET surface area and the pore size distributions were calculated by using the Brunauer Emmett Teller (BET) method and Barrett Joyner Halenda (BJH) desorption curve analysis, respectively.

2.3 Synthesis of hollow carbon nanoparticles (HC)

TEAOH (9.98 mL), deionized water (1.87 mL) and $NaAlO_2$ (170 mg) were successively added into the beaker and mixed evenly under magnetic stirring. After stirring for 1 h, fumed silica (2.4 g) was added to the mixture to react for 2 h, and then transferred into Teflon-lined stainless steel autoclave for aging for 30 h at 140 °C. The product was cooled to room temperature, centrifuged and washed with deionized water. The TEAOH was removed by high temperature calcination to obtain nano-beta zeolite. Then, the nano-beta zeolite (60 mg) was completely dissolved in deionized water (3 mL), BMIMBr (10 mg) was added, sonicated for 30 minutes and then stirred for 2 h at room temperature. After centrifugation, water washing and vacuum drying at 50 °C, the product was collected, heated to 300 °C at a rate of 5 °C min^{-1} through a tube furnace under a nitrogen atmosphere for 1 h, and then heated from 300 °C to 800 °C at a rate of 10 °C min^{-1} for 1 h. After calcination at high temperature, the carbonized product beta-C nanomaterials were obtained. Afterwards, the beta-C were dissolved in deionized water to obtain 5 mL of beta-C solution with a concentration of 2 mg mL^{-1} and 0.5 mL of NaOH solution (2 M) was added to stir for 12 h. The HC nanoparticles were collected after centrifugation and water washing.

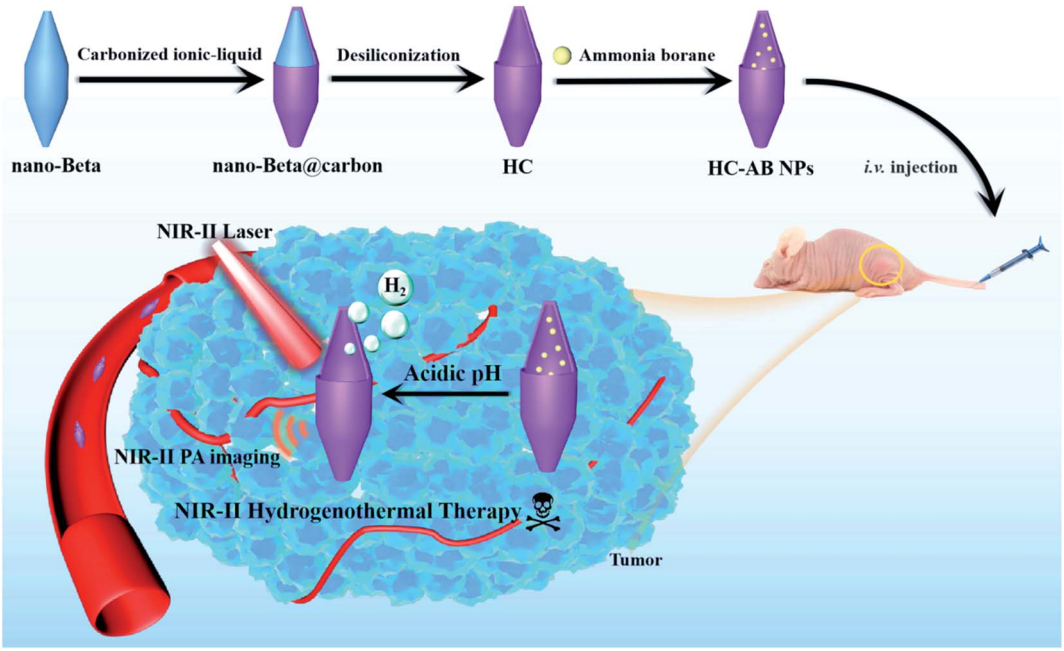

Scheme 1 Schematic illustration of preparation of HC-AB NPs and their therapeutic mechanism.

2.4 Synthesis of hollow carbon-ammonia borane nanoparticles (HC-AB NPs)

HC nanoparticles (5 mg) was dissolved in deionized water (5 mL), and then AB (25 mg) was added to stir for 2 h. The final products were collected after centrifugation and water washing for several times to obtain HC-AB NPs.

2.5 *In vitro* photothermal test

A 1064 nm laser with a power density of 1.0 W cm^{-2} was used to irradiate different concentrations of HC-AB solution (0.2 mL) for 5 min, and the temperature change was recorded with an infrared thermal image (Fluke Ti400).

2.6 Hydrogen release

HC-AB solution (50 μL, 200 μg mL^{-1}) was dripped onto the slide and covered with a cover slip. After adding buffers with different pH values on the edge of the cover slip, the generation and growth of H_2 bubbles were observed through an inverted laser scanning microscope (OLYMPUS DP80). Furthermore, we also observed the generation and growth process of H_2 bubbles in HC-AB solution under the irradiation of 1064 nm laser at pH = 5.6 by the above method.

2.7 Cytotoxicity assay

4T1 cells line was acquired from the Type Culture Collection of the Chinese Academy of Sciences (Shanghai, China) and cultured in DMEM (Dulbecco's modified Eagle's medium) containing 10% (v/v) fetal bovine serum (FBS) and 1% antibiotics (penicillin–streptomycin) (Corning) at 37 °C under 5% CO_2 atmosphere. The cytotoxicity of HC-AB NPs in the absence/presence of laser irradiation was evaluated by a standard Cell Counting Kit (CCK-8) (Sigma-Aldrich, St. Louis, MO, USA) assay. A density of 1.0×10^4 4T1 cells per well was seeded in 96-well plates for 12 h at 37 °C and incubated with different concentrations of HC-AB NPs. In the laser-irradiated group, the cells were irradiated with 1064 nm laser (1 W cm^{-2}) for 5 min. The CCK-8 solution (10 μL, 5 mg mL^{-1}) was added into the 96-well plate along with the culture medium, and incubate for 2 h. Then, a microplate reader (BioTek Epoch 2) was used to measure.

2.8 *In vitro* cellular uptake test

4T1 cells were incubated with HC-AB NPs (200 μg mL^{-1}) for 24 h. Then, the cells were collected, fixed and sectioned for bio-TEM observation.

2.9 Trypan blue staining assay

4T1 cells (1.0×10^4 cells per well) were seeded into a 48-cell plate and incubated for 24 h. Then, the medium containing PBS, HC (200 μg mL^{-1}) and HC-AB (200 μg mL^{-1}) was added and incubated for 6 h. After replacing with fresh medium, irradiate cells with or without NIR-II laser (1064 nm, 1 W cm^{-2}) for 5 min. After incubation for 4 h, the cells were washed with PBS and stained with trypan blue. Finally, observing through a microscope (LEICA DFC450 C).

2.10 Animal models

All live animal experiments were conducted according to the protocols approved by the Institutional Animal Care and Use Committee of the Animal Experiment Center of Shanxi Medical University (2016LL141, Taiyuan, China). Female Balb/c nude mice (6–8 weeks old, 17–19 g) were purchased from

Weitong Lihua Experimental Animal Technology Co. Ltd (Beijing). After mice were acclimated to the animal facility for at least 7 days, each was injected with 1×10^6 4T1 cells on the left-back to obtain the tumor model. The mice have used experiments when the tumor volume approached 80–100 mm^3.

The tumor-bearing mice were injected intravenously with solutions (PBS, HC and HC-AB). 6 h after the injection, 1064 nm laser (1 W cm^{-2}) was irradiated for 5 min. After 12 h, blood was collected from these mice, and the pro-inflammatory cytokines (IL-6, IL-1β and TNF-α) were measured using the Elisa analysis method.

2.11 PA imaging

HC-AB NPs were configured as an aqueous solution of various concentrations and acquired the *in vitro* NIR-II PA images using real-time multispectral optoacoustic tomographic (MSOT) imaging system. For *in vivo* imaging, tumor-bearing mice were injected intravenously with the solutions. The NIR-II PA images of these mice were obtained for different periods (before injection and 1, 4, 6, and 24 h after injection).

2.12 *In vivo* photothermal/gas synergistic therapy

Tumor-bearing mice were divided into six groups and treated with PBS, PBS + Laser, HC, HC + Laser, HC-AB, HC-AB + Laser. After 6 h injection, the mice requiring laser irradiation were anesthetized and irradiated using a 1064 nm NIR laser (1 W cm^{-2}) for 5 min. The temperature changes were obtained by an infrared camera (Fluke Ti400). Tumor volume, body weight and photographs of all mice were recorded every two days.

2.13 Histology analysis

The tumors were obtained from the mice in each group. Histology analysis of these tissues by H&E staining.

3. Results and discussion

Transmission electron microscopic (TEM) images clearly demonstrate that the synthesized HC-AB NPs exhibited a hollow sphere-like morphology and uniform particle size of ~200 nm (Fig. 1a). The hollow NPs have a clear shell structure with an average shell thickness in the range of 37.5 nm (Fig. 1b). The energy dispersive spectroscopy (EDS) line scan analysis chart (Fig. 1c) showed the homogeneous distribution of C and N elements in HC-AB NPs. Specific surface area and average pore size distribution of HC-AB NPs were 426.5404 m^2 g^{-1} and 5.6 nm, respectively (Fig. 1d and inset), which indicated its potential as an effective nanocarrier. Notably, the particle size of HC-AB NPs have no obvious difference after loading the AB, and the zeta potential changed from −25.8 to −35.8 mV (Fig. S1 and S2, ESI†). Compared with the HC, the peak of FT-IR spectrum at 1381, 2285, 2343 and 2389 cm^{-1} (Fig. 1e) could demonstrate the successful loading of AB in the HC-AB NPs. In addition, as shown in Fig. 1f, the C 1 s spectrum can be divided into the following different types of peaks, C–C (284.8 eV), C–O (286.72 eV), C═N (287.19 eV), C═O and C–N (288.99 eV).[40] These results together indicate the successful preparation of HC-AB NPs.

The excellent adsorption properties of the HC-AB NPs (Fig. 2a and S3, ESI†), especially in the NIR-II region indicated that the HC-AB NPs could be used as a potential NIR-II photosensitizer, which encouraged us to explore the NIR-II PTT performance of HC-AB NPs by supervising the rise of

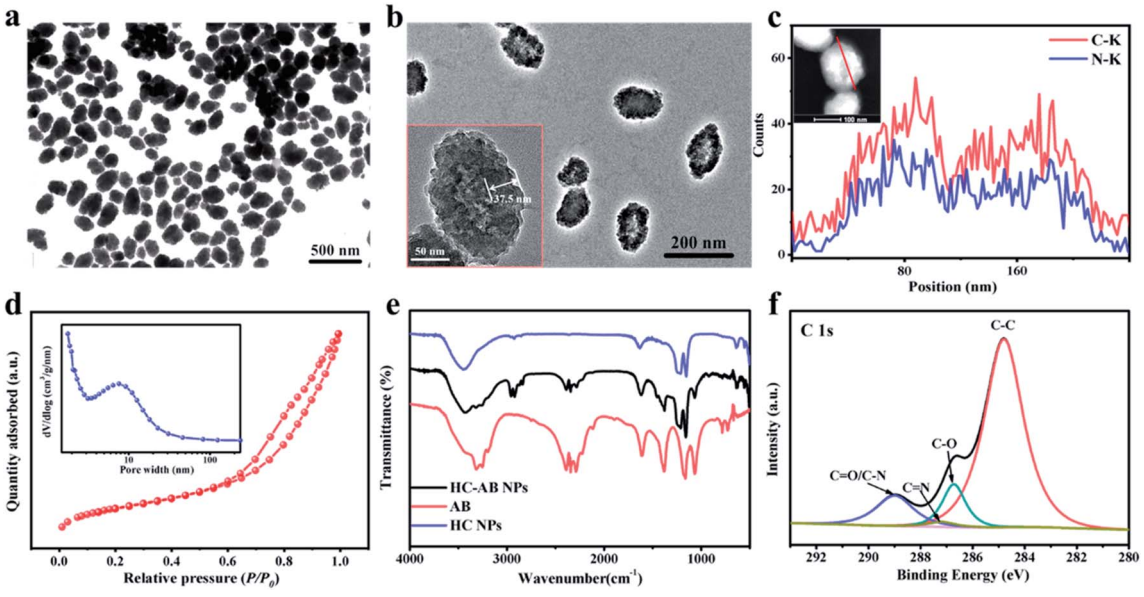

Fig. 1 Characterization of HC-AB NPs. (a) TEM image and (b) HR-TEM image of HC-AB NPs. (c) EDS line scan analysis of HC-AB NPs. (d) Nitrogen adsorption–desorption isotherm of HC-AB NPs, where the insert is the pore size distribution curve. (e) FT-IR spectra and (f) XPS spectrum of HC-AB NPs.

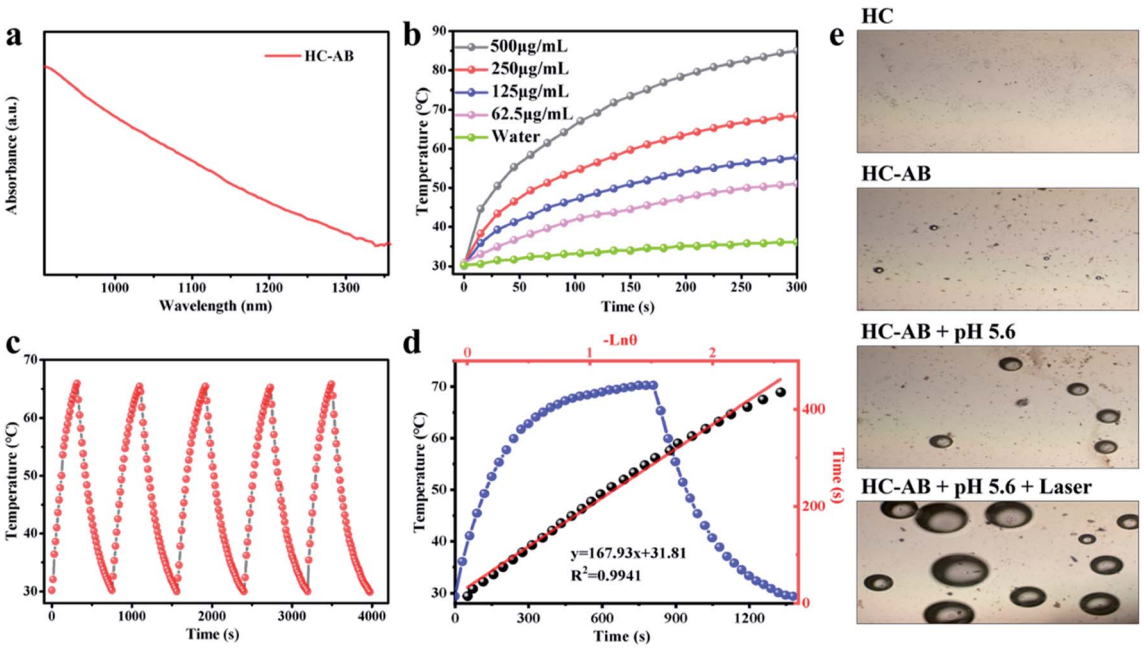

Fig. 2 (a) Adsorption spectrum of HC-AB NPs in NIR-II. (b) Heating curves of HC-AB with different concentrations under laser irradiation (1064 nm, 1.0 W cm^{-2}). (c) Five on–off cycles of NIR irradiation for HC-AB solutions. (d) Photothermal conversion efficiency of HC-AB NPs. (e) H_2 release of HC-AB NPs with or without laser irradiation under different pH conditions.

temperature and photothermal stability upon the 1064 nm laser irradiation. As described in Fig. 2b, the temperature changes of HC-AB solutions showed significant concentration dependence. After 5 min of irradiation, the temperature of 0.5 mg mL^{-1} HC-AB solution can reach 85 °C, by contrast, the temperature of PBS increased by only 37.4 °C in the same condition. The photothermal stability was another vital factor of photothermal therapy agent. Therefore, the temperature elevation of HC-AB solution was maintained upon laser irradiation for 5 on/off cycles. The thermal characteristics of HC-AB NPs did not change under repeated laser irradiation (Fig. 2c). In addition, according to the obtained data, the photothermal conversion efficiency (η) of HC-AB was up to 25.45%, which is slightly higher than reported related literature (Fig. 2d).[41] Inspired by the excellent NIR-II photothermal conversion performance of HC-AB NPs and the efficient hydrogen storage performance of AB, the effect of the different conditions on H_2 release was evaluated (Fig. 2e). When the pH reached 5.6 and laser irradiation, the release of H_2 has increased significantly. The result indicated that in the tumor microenvironment, the HC-AB NPs is expected to achieve a responsive release of H_2 under the synergistic effect of low pH and NIR-II light irradiation.

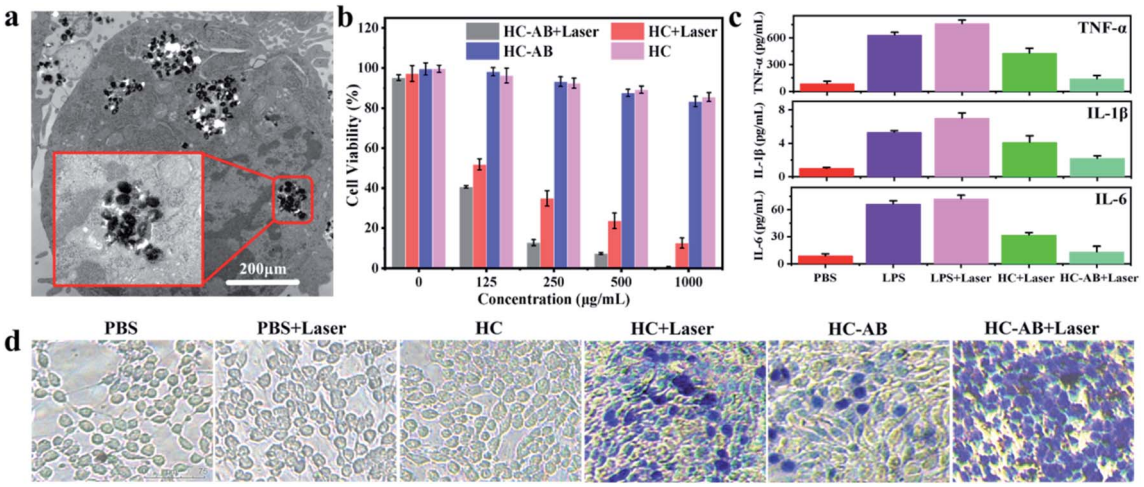

Fig. 3 (a) Cell uptake of NMs (Bio-TEM image of 4T1 cells incubated with HC-AB for 24 h) (b) cell viability after HC-AB NPs treatment of 4T1 cells with or without laser (1064 nm, 1 W cm^{-2}) irradiation. (c) After different treatments, the levels of pro-inflammatory cytokines (TNF-α, IL-1β and IL-6). (d) Microscopic photos of 4T1 cells stained by trypan blue after different treatments.

Due to the excellent performance of HC-AB NPs in NIR-II photothermal conversion and H_2 release, HC-AB NPs are considered as a novel tumor nanotherapeutic agent. To confirm this possibility, the cellular uptake of HC-AB NPs was firstly detected by TEM images. As shown in Fig. 3a, the HC-AB NPs can be effectively endocytosed by 4T1 cells after 2 h incubation time. The biocompatibility and photothermal ablation efficacy of HC-AB NPs *in vitro* was tested using the standard cell counting kit 8 (CCK-8). As shown in Fig. 3b, the cell 4T1 viability decreased slightly with the increase of HC-AB NPs concentration. However, the cell survival rate remained above 85% when the concentration of HC-AB NPs is as high as 1 mg mL^{-1}, predicting the low cytotoxicity and the great biocompatibility of HC-AB NPs. However, the cell survival rate was significantly declined when 4T1 cells were incubated with the same amount of HC-AB NPs following 1064 nm laser irradiation (1 W cm^{-2}) for 5 min, and the survival rate was more significantly decreased in the HC-AB than that of HC group, indicating that the HC-AB NPs could be excellent photothermal ablation nanoagent for cancer.

The anti-inflammatory effect of released H_2 on the RAW 264.7 macrophages was examined, LPS-induced inflammatory response was used as a control. As shown in Fig. 3c, compared with the PBS + laser group, the levels of proinflammatory cytokines (TNF-α, IL-1β, and IL-6) in the HC + laser group were significantly increased. Specifically, the changes in the HC-AB + laser group were relatively small, indicating that the HC-AB + laser can reduce the inflammatory damage caused by PTT. Due to the increased permeability of the cell membrane of dead cells, it can be dyed blue by trypan blue, the apoptosis of 4T1 cells after different treatments was observed by trypan blue staining. As shown in Fig. 3d, compared with the HC-AB group and the HC + laser group, the number of damaged 4T1 cells increased significantly in the HC-AB + laser group, indicating that HC-AB NPs exhibit stronger toxicity under laser irradiation and can increase tumor cell apoptosis.

Based on the superior NIR-II absorption performance of HC-AB NPs, the *in vitro* NIR-II PA imaging of HC-AB NPs was tested (Fig. 4a). As expected, the PA intensity increases with increasing solution concentration. Inspired by the good imaging results of HC-AB NPs *in vitro*, we further explored the NIR-II PA imaging performance *in vivo*. The HC-AB NPs was injected into the 4T1 tumor-bearing mice through the tail vein, and NIR-II PA images were recorded before and after the injection (1 h, 4 h, 6 h, and 24 h, respectively) (Fig. 4b). No obvious NIR-II PA signal was observed in mice before injection. The PA intensity at the tumor site gradually increased over time and reached the maximal retention at 6 h after HC-AB injection. Moreover, the analysis of PA intensity further revealed that the maximal accumulation of HC-AB NPs presented at 6 h, which could be selected as the optimal time for cancer diagnosis and treatment.

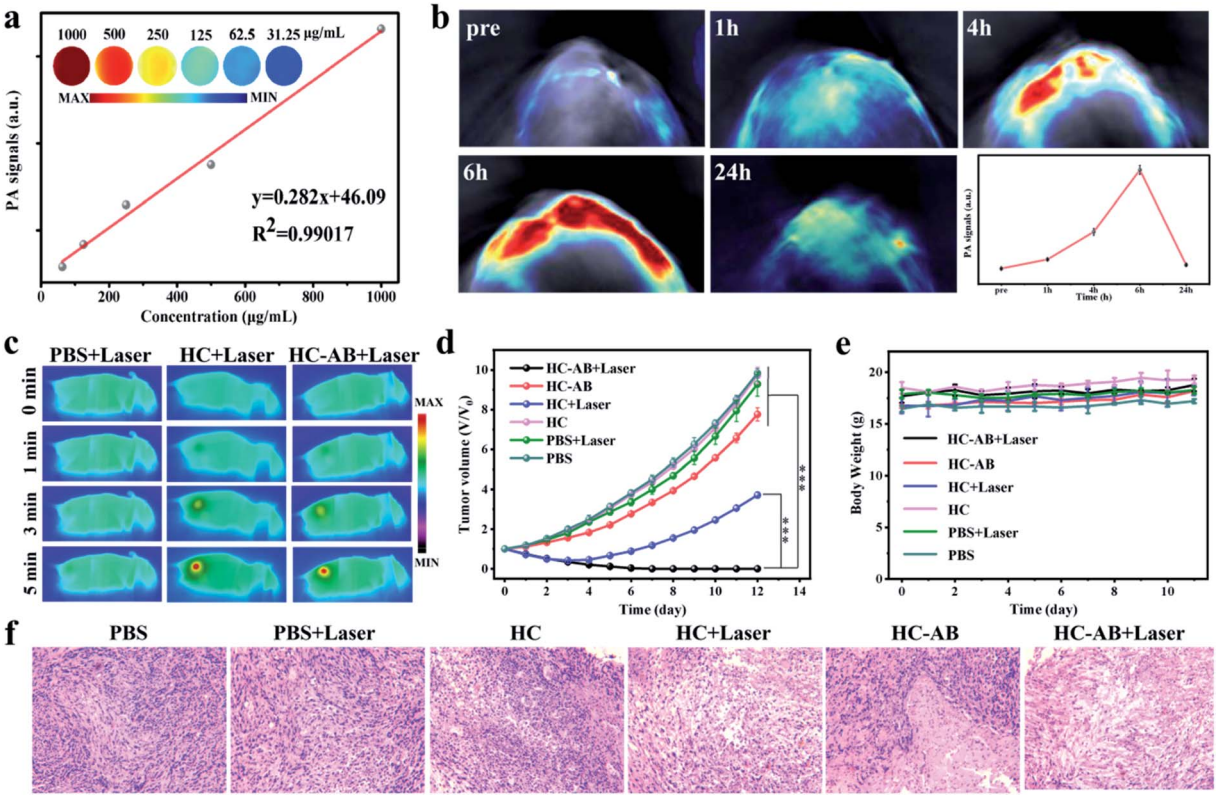

Fig. 4 (a) NIR-II PA imaging and the corresponding quantitative concentration-dependent photoacoustic values of HC-AB NPs. (b) NIR-II PA imaging of tumor-bearing mice with intravenous injection of HC-AB NPs within 24 h. (c) Infrared thermal images of different treatments with NIR-II irradiation (1064 nm, 1 W cm^{-2}). (d) Tumor growth curves and (e) body weight changes of tumor-bearing mice after various treatment. (f) H&E stained tumor slices collected from mice at the end of treatment.

Based on the excellent tumor accumulation and photothermal properties, the *in vivo* anti-tumor efficacy of the HC and HC-AB NPs was evaluated through the 4T1 tumor-bearing mice model. The 4T1 tumor-bearing mice were intravenously administered with PBS, HC and HC-AB NPs (15 mg kg^{-1}) using the NIR-II laser (1064 nm, 1 W cm^{-2}) for 5 min after 6 h injection. Compared with the control group (PBS + laser), the temperature of tumor sites could be increased to above 49 °C in the other two groups (Fig. 4c), this temperature can well eliminate tumor cells.

To further prove the effect of hydrogenothermal synergistic therapy, the tumor-bearing 4T1 mice were divided into six groups (PBS, PBS + laser, HC, HC + Laser, HC-AB, and HC-AB + Laser). After that, for these six groups of tumor-bearing mice, detailed tumor dynamic changes and body weight were recorded every two days for 2 weeks (Fig. 4d and e). For groups requiring laser irradiation, six hours after injection of PBS, HC, or HC-AB, the tumor site of mice was irradiated with 1064 nm laser located in the NIR-II. The HC and HC-AB groups without laser irradiation showed an indistinctive antitumor effect compared to the PBS group. Notably, compared with the other groups, no tumor relapse was observed for the HC-AB + laser group. These results indicate that NIR-II hydrogenothermal treatment is more effective than simple NIR-II PTT. Importantly, no obvious variations in the body weight of all mice further confirmed that the HC-AB NPs have good biocompatibility and low toxicity. Moreover, the hematoxylin and eosin (H&E) staining analysis (Fig. 4f), which was carried out for tumors collected from the six groups, showed significant tumor damage in the PTT treatment of HC-AB + laser group. Overall, the above results indicated that the hydrogenothermal therapy by the HC-AB NPs can realize an excellent anti-tumor efficacy, which offers a promising avenue for clinical treatment.

4. Conclusions

In summary, we developed the HC-AB NPs, a nanotheranostic platform based on NIR-II, used for diagnosis and treatment of tumors. The synthesized HC-AB NPs have excellent light-to-heat conversion rate under NIR-II laser irradiation, so as to perform PA imaging and PTT. After the HC-AB NPs reached the tumor sites, due to the weak acidic environment of the tumor cells, the loaded AB could released H_2 for gas therapy. Specifically, the heat generated during the NIR-II PTT could accelerate the release of H_2, so as to carry out synergistic hydrogenothermal therapy, further enhance the anti-tumor efficacy of NPs. The developed HC-AB NPs provide a feasible way to the proposed NIR-II hydrogenothermal therapy strategy by combination of hydrogen gas therapy and NIR-II PTT would open a new window for cancer therapy.

Conflicts of interest

The authors declare that they have no known competing financial interests or personal relationships that could have appeared to influence the work reported in this paper.

Acknowledgements

This work was supported by the National Natural Science Foundation of China (No. 81571747, 81771907), Science and technology innovation team project of Shanxi Province (No. 201705D131026), Engineering Technology Research Center of Shanxi Province (No. 201805D121008), Scientific and technological achievements transformation project of Shanxi Province (No. 201704D131006), Laboratory Construction Project of Shanxi Province, The Projects for Local Science and Technology Development Guided by the Central Committee (YDZX20191400002537), Scientific and Technological Innovation Programs of Higher Education Institutions in Shanxi (2019L0415), Shanxi Province Science Foundation for Youths (201901D211343).

References

1 H. Chen, X. Zhou and Y. Gao, *Drug discovery today*, 2014, **19**, 502.
2 D. D. De. Silva, S. Rapior and F. Fons, *Fungal Divers.*, 2012, **55**, 1.
3 L. Xu, L. Cheng and C. Wang, *Polym. Chem.*, 2014, **5**, 1573.
4 K. Yang, L. Hu and X. Ma, *Adv. Mater.*, 2012, **24**, 1868.
5 X. Huang X and M. A. El-Sayed, *Alexandria J. Med.*, 2011, **47**, 1.
6 Z. Zhang, J. Wang and C. Chen, *Adv. Mater.*, 2013, **25**, 3869.
7 K. Yang, J. Wan and S. Zhang, *Biomaterials*, 2012, **33**, 2206.
8 F. Zhou, S. Wu and Y. Yuan, *Small*, 2012, **8**, 1543.
9 J. T. Robinson, S. M. Tabakman and Y. Liang, *J. Am. Chem. Soc.*, 2011, **133**, 6825.
10 Y. Jiang, J. Li and X. Zhen, *Adv. Mater.*, 2018, **30**, 1705980.
11 J. Y. Kim, W. I. Choi and M. Kim, *J. Controlled Release*, 2013, **171**, 113.
12 S. Zhu, R. Tian and A. L. Antaris, *Adv. Mater.*, 2019, **31**, 1900321.
13 O. T. Bruns, T. S. Bischof and D. K. Harris, *Nat. Biomed. Eng.*, 2017, **1**, 1.
14 H. Lin, S. Gao and C. Dai, *J. Am. Chem. Soc.*, 2017, **139**, 16235.
15 Y. Lyu, J. Li and K. Pu, *Small Methods*, 2019, **3**, 1900553.
16 B. Guo, Z. Sheng and D. Hu, *Adv. Mater.*, 2018, **30**, 1802591.
17 X. Ding, C. H. Liow and M. Zhang, *J. Am. Chem. Soc.*, 2014, **136**, 15684.
18 B. Han, Y. L. Zhang and Q. D. Chen, *Adv. Funct. Mater.*, 2018, **28**, 1802235.
19 K. D. Patel, R. K. Singh and H. W. Kim, *Mater. Horiz.*, 2019, **6**, 434.
20 X. Zhang, J. Du and Z. Guo, *Adv. Sci.*, 2019, **6**, 1801122.
21 W. Xu, J. Qian and G. Hou, *Acta Biomater.*, 2019, **83**, 400.
22 X. Qiu, L. Xu and Y. Zhang, *Mol. Pharmaceutics*, 2016, **13**, 829.
23 G. Wan, B. Chen and L. Li, *Biomaterials*, 2018, **155**, 25.
24 L. Feng, D. Yang and S. Gai, *Chem. Eng. J.*, 2018, **351**, 1147.
25 W. Fan, B. Yung and P. Huang, *Chem. Rev.*, 2017, **117**, 13566.
26 Q. Xiao, X. Zheng and W. Bu, *J. Am. Chem. Soc.*, 2013, **135**, 13041.
27 W. Sang, Z. Zhang and Y. Dai, *Chem. Soc. Rev.*, 2019, **48**, 3771.
28 Y. Wang, H. Wang and D. Liu, *Biomaterials*, 2013, **34**, 7715.

29 C. Szabo, *Nat. Rev. Drug Discovery*, 2016, **15**, 185.
30 L. Yu, P. Hu and Y. Chen, *Adv. Mater.*, 2018, **30**, 1801964.
31 O. Kabil, V. Vitvitsky and R. Banerjee, *Annu. Rev. Nutr.*, 2014, **34**, 171.
32 Y. Wu, M. Yuan and J. Song, *ACS Nano*, 2019, **13**, 8505.
33 D. Laveti, M. Kumar and R. Hemalatha, *Inflamm. Allergy - Drug Targets*, 2013, **12**, 349.
34 C. Zhang, D. W. Zheng and C. X. Li, *Biomaterials*, 2019, **223**, 119472.
35 T. T. V. Phan, T. C. Huynh and P. Manivasagan, *Nanomaterials*, 2020, **10**, 66.
36 Y. Kotsuchibashi, Y. Nakagawa, and M. Ebara, *Biomaterials Nanoarchitectonics*, 2016,vol. 7.
37 H. Wu, H. Jiang and Y. Yang, *J. Mater. Chem. A*, 2020, **8**(29), 14498–14505.
38 T. J. Kim, J. H. Yoon and G. R. Yi, *Nanoscale*, 2019, **11**, 13650.
39 T. Yang, Z. Jin and Z. Wang, *Appl. Mater. Today*, 2018, **11**, 136.
40 C. Liao, B. Liu and Q. ChiQ, *ACS Appl. Mater. Interfaces*, 2018, **10**, 44421.
41 H. Wang, X. Pan and X. Wang, *ACS Nano*, 2020, **14**, 2847.